JACS
JOURNAL OF THE AMERICAN CHEMICAL SOCIETY
pubs.acs.org/JACS
Article

Nuclear Quantum Effects Prolong Charge Carrier Lifetimes in Hybrid Organic−Inorganic Perovskites

Yulong Liu, Run Long,* Wei-Hai Fang, and Oleg V. Prezhdo

Cite This: J. Am. Chem. Soc. 2023, 145, 14112−14123
Read Online

ABSTRACT: Hybrid organic−inorganic perovskites (HOIPs) contain light hydrogen atoms that exhibit significant nuclear quantum effects (NQEs). We demonstrate that NQEs have a strong effect on HOIP geometry and electron−vibrational dynamics at both low and ambient temperatures, even though charges in HOIPs reside on heavy elements. By combining ring-polymer molecular dynamics (MD) and ab initio MD with nonadiabatic MD and time-dependent density functional theory and focusing on the most studied tetragonal $CH_3NH_3PbI_3$, we show that NQEs increase the disorder and thermal fluctuations through coupling of the light inorganic cations to the heavy inorganic lattice. The additional disorder induces charge localization and decreases electron−hole interactions. As a result, the nonradiative carrier lifetimes are extended by a factor of 3 at 160 K and 1/3 at 330 K. The radiative lifetimes are increased by 40% at both temperatures. The fundamental band gap decreases by 0.10 and 0.03 eV at 160 and 330 K, respectively. By enhancing atomic motions and introducing new vibrational modes, NQEs strengthen electron−vibrational interactions. Decoherence, determined by elastic scattering, accelerates almost by a factor of 2 due to NQEs. However, the nonadiabatic coupling, driving nonradiative electron−hole recombination, decreases because it is more sensitive to structural distortions than atomic motions in HOIPs. This study demonstrates, for the first time, that NQEs should be considered to achieve an accurate understanding of geometry evolution and charge carrier dynamics in HOIPs and provides important fundamental insights for the design of HOIPs and related materials for optoelectronic applications.

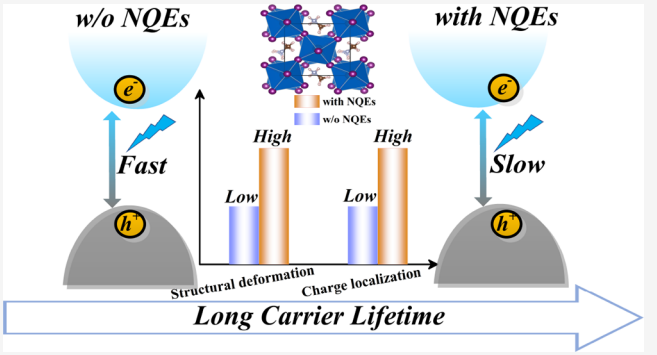

1. INTRODUCTION

Low cost and outstanding performance,[1,2] arising due to excellent defect tolerance,[3,4] high absorption coefficient,[5] long charge carrier diffusion,[6−8] and slow electron−hole recombination,[9] have stimulated intense research efforts on hybrid organic−inorganic halide perovskite (HOIP) solar cells, which have witnessed rapid growth in the photovoltaic conversion efficiency from 3.81[10] to 25.7%[11] within only a decade of development. HOIPs are also used in lasers,[12] photodetectors,[13,14] light-emitting diodes,[15,16] field-effect transistors,[17] and other optoelectronic devices.[18−21] Nonradiative electron−hole recombination still limits the performance of these devices because it constitutes a major route for charge and energy losses. Many significant efforts[22−31] have been dedicated to the investigation of nonradiative relaxation in order to establish its atomistic mechanisms and to propose rational strategies to minimize nonradiative losses. Thus far, all the simulations have treated atomic motions classically, neglecting nuclear quantum effects (NQEs) that can be pronounced in HOIPs, such as $MAPbI_3$ ($MA = CH_3NH_3^+$), in the presence of light hydrogen atoms. Although charge carriers are supported by the inorganic lattice formed by heavy Pb and I atoms and the electron and hole wavefunctions have no contributions from the organic component, the organic species couple strongly to the inorganic ionic lattice through both short-ranged steric and long-ranged electrostatic interactions and influence electron−hole and charge−phonon interactions.[23−26]

Many works have shown substantial NQEs in hydrogen-containing systems associated with quantum tunneling of protons and zero-point motion of chemical bonds involving hydrogen atoms.[32−42] For example, NQEs modulate hydrogen bond interactions.[35−37,43−45] Given the strong correlation between motions of the organic and inorganic components of HOIPs,[23−26] including hydrogen bonding,[46] one can expect that NQEs influence HOIP geometric and electronic properties as well as charge carrier dynamics. Typically, NQEs are more pronounced at low than high temperatures because high

Received: April 28, 2023
Published: June 19, 2023

https://doi.org/10.1021/jacs.3c04412
J. Am. Chem. Soc. 2023, 145, 14112−14123

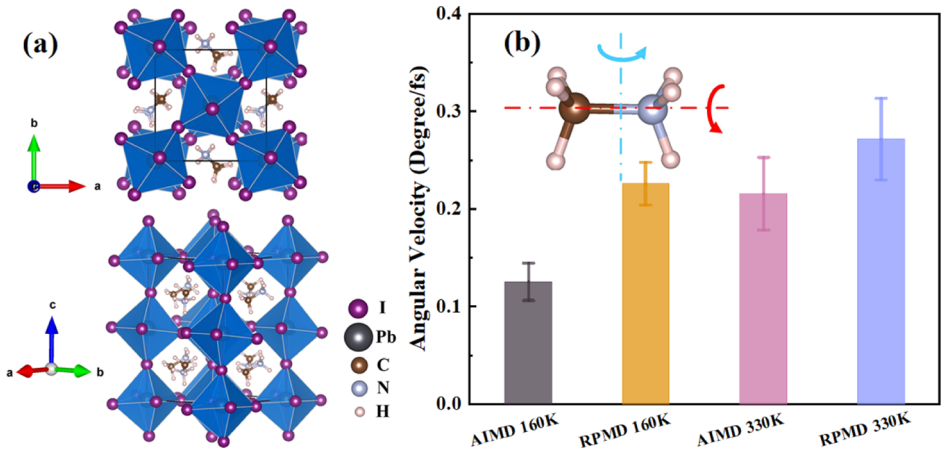

Figure 1. (a) Optimized tetragonal $MAPbI_3$ geometric structure. (b) Canonically averaged ARAV of MA cations (inset), extracted from the AIMD and RPMD trajectories of $MAPbI_3$ at 160 and 330 K. The rotation is faster when NQEs are included via RPMD. The error bars characterize fluctuations of the angular velocity. The fluctuation is larger at higher temperatures and upon inclusion of NQEs. Although MA cations do not contribute to the electron and hole wavefunctions near the band edges of $MAPbI_3$, their motions affect the electron−hole and charge−vibrational interactions indirectly.

temperatures put systems in the classical limit.[32−42] HOIP solar cells and other devices operate at different temperatures, and therefore it is important to study NQEs over a temperature range. In this regard, the tetragonal phase of $MAPbI_3$ is an excellent system to study the temperature-dependent influence of NQEs on the geometric and electronic properties of HOIPs and the nonradiative electron−hole recombination dynamics because the phase remains stable in the range between 160 and 330 K, including both low and ambient temperatures.

In this work, we investigate structural and electronic properties, electron−vibrational interactions, and radiative and nonradiative charge carrier recombination in tetragonal $MAPbI_3$ at 160 and 330 K with and without NQEs. For this purpose, we employ ring-polymer molecular dynamics (RPMD) to include NQEs[33,34] and ab initio molecular dynamics (AIMD) to treat atoms classically. To study the charge carrier recombination, we combine AIMD and RPMD with nonadiabatic molecular dynamics (NA-MD)[44,47−54] and real-time time-dependent density functional theory (TD-DFT).[55,56] The simulations show that NQEs enhance fluctuations of the MA cations, in particular since they contain light hydrogen atoms. Even though the MA cations do not contribute to the $MAPbI_3$ electronic wavefunctions in the relevant energy range, they influence the electronic properties, electron−vibrational interactions, and interaction with light indirectly by coupling to the Pb−I inorganic lattice sterically, via hydrogen bonding, and by long-range electrostatic interactions with the charges. Significant NQEs are seen at both low and ambient temperatures. By enhancing the motion of the MA cations, NQEs increase structural distortions that localize electrons and, particularly, holes. As a result, the nonadiabatic coupling (NAC) and the optical transition dipole moment are reduced, and the nonradiative and radiative excited-state lifetimes are increased. By enhancing atomic fluctuations and introducing new vibrational motions, NQEs speed up phonon-induced coherence loss within the electronic subsystem. The fundamental band gap decreases by 30−100 meV due to NQEs. The distributions of the key structural features are broadened. The Pb−I bond length grows by 0.1 Å as the I−I−I angle between $[PbI_6]^{4-}$ octahedra increases, while the I−Pb−I angle describing the shape and distortion of a single $[PbI_6]^{4-}$ octahedron decreases. Particularly, being strong at low temperatures, NQEs persist at ambient temperatures and above, indicating that they should be considered when studying HOIP properties for most applications. The detailed analysis rationalizes the influence of NQEs on $MAPbI_3$ properties and charge dynamics and provides fundamental insights into the unusual properties of HOIPs for the design of solar cells and other optoelectronic devices.

2. RESULTS AND DISCUSSION

2.1. Geometric Structure. Figure 1a shows the optimized geometry of $MAPbI_3$ in the tetragonal phase (space group: *I*4/*mcm*). The optimized lattice parameters $a = b = 8.800$ Å and $c = 13.047$ Å are in good agreement with the calculated and experimental values.[57−59] To examine the influence of NQEs and thermal effects on the geometry and electron−phonon interaction, we computed the average absolute rotational angular velocity (ARAV) of MA cations using the AIMD and RPMD trajectories at 160 and 330 K. Figure 1b demonstrates that ARAV increases in the sequence: AIMD 160 K (0.125°/fs) < AIMD 330 K (0.216°/fs) < RPMD 160 K (0.226°/fs) < RPMD 330 K (0.272°/fs). At the lower temperature of 160 K, NQEs increase the ARAV by almost a factor of 2 relative to the AIMD value. At 330 K, NQEs increase the ARAV by about a quarter. NQEs enhance MA motions, which, in turn, enhance motions of the inorganic lattice due to the correlation between the inorganic and organic components of HOIPs.[24−26] NQEs are more significant at lower temperatures, as expected. The higher temperature also enhances motions of the classical atoms, leading to more pronounced structural distortion and stronger atomic fluctuations.[23]

To provide a visualization of the temperature-dependent NQEs, we superimposed snapshots of the 3 ps AIMD and RPMD trajectories at 160 and 330 K, Figure 2. At a lower temperature of 160 K, the Pb and I atoms fluctuate around their equilibrium positions, while the MA cations move significantly within the space provided by the inorganic lattice, particularly when NQEs are included, Figure 2a,b. When the temperature is increased to 330 K, the movements of Pb and I grow mildly, while the MA cations fluctuate even more

https://doi.org/10.1021/jacs.3c04412
J. Am. Chem. Soc. 2023, 145, 14112−14123

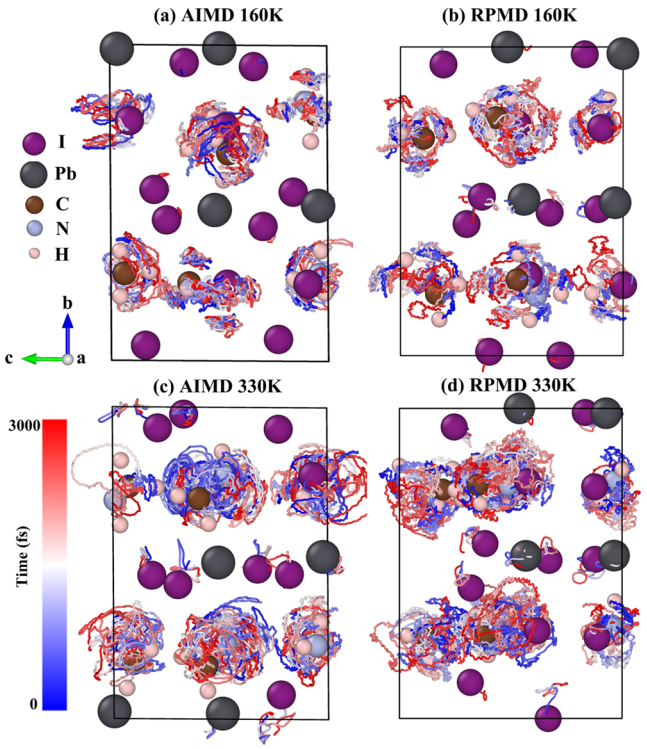

Figure 2. Superimposed images representing the motion of $MAPbI_3$ during the 3 ps trajectories obtained with (a) AIMD and (b) RPMD at 160 K and (c) AIMD and (d) RPMD at 330 K. The MA cations move significantly faster than the Pb and I atoms at both low and high temperatures. The movement is enhanced by NQEs.

compared to the lower temperature. Again, NQEs enhance MA movements. The qualitative picture illustrated in Figure 2 is quantified by the data in Figures 1 and 3.

To identify the temperature-dependent influence of NQEs on geometry distortion and atomic motions, we analyze three important geometric features,[24,60] including the I−I−I angle, the equatorial I−Pb−I angle, and the Pb−I bond length. The distributions are plotted in Figure 3. The I−I−I angle controls the orientation of adjacent $[PbI_6]^{4-}$ octahedra with respect to each other. The equatorial I−Pb−I angle reflects the shape of a $[PbI_6]^{4-}$ octahedron. The Pb−I bond length characterizes motions of atoms with respect to each other. It has been shown that geometry deformation has a stronger influence on the electronic properties and electron−vibrational interactions than ionic motions.[24,60,61] The distributions of the three features are broader in the presence of NQEs than without NQEs at both 160 and 330 K, indicating that NQEs indeed enhance the structural distortion. The calculated average I−I−I angle increases from 92.466° (AIMD) to 94.337° (RPMD) at 160 K, a 2.02% increase. Note that even though NQEs should be important for the light H-atoms, the structural parameters associated with the heavy elements change as well. When the temperature is raised to 330 K, the I−I−I angle grows from 93.206° (AIMD) to 94.984° (RPMD), a 1.91% growth. Thus, NQEs are more pronounced at lower temperatures than at higher temperatures. This remains true for the Pb−I bond length, whose average value is 3.190 Å (AIMD) and 3.256 Å (RPMD) at 160 K, a 2.07% increase. The corresponding increase is only 0.986% at 330 K from 3.244 Å in the AIMD simulation to 3.276 Å in the RPMD simulation. In comparison, the equatorial I−Pb−I angle decreases with both increasing temperature and the inclusion of NQEs. The I−Pb−I angle decreases from 155.285° (AIMD) to 154.654° (RPMD) at 160 K and from 152.525° (AIMD) to 149.450° (RPMD) at 330 K. The corresponding relative changes are 0.406 and 2.02% at 160 and 330 K, respectively. That is NQEs have a stronger influence on the shape of the $[PbI_6]^{4-}$ octahedron at higher temperatures. Not expected a priori, this result highlights the often-unusual influence of thermal effects on the HOIP structure and dynamics.[62−66] Overall, an increased temperature increases structural disorder, which is further enhanced by NQEs. Generally, the influence of NQEs on the structural distortion and atomic motions is more important at the lower temperature and becomes less important at higher temperatures. The structural disorder inevitably has an impact on the electron−hole interaction, NAC, and charge carrier lifetimes. Changes in the Pb−I interatomic interactions are caused by temperature, and NQEs influence electron−vibrational interactions and electron−hole recombination. In the present case, zero-point motion constitutes the main NQE because it broadens the distribution of coordinates of light hydrogen atoms. Quantum tunneling plays a less important role because hydrogen atoms do not need to overcome important energy barriers.

To characterize the atomic fluctuations quantitatively, we computed standard deviations of the relative displacements of atoms in the MA cations and the H, Pb, and I atoms, according to $\sigma_i = \sqrt{\langle(\vec{r}_i - \langle\vec{r}_i\rangle)^2\rangle}$. Here, $\vec{r}_i$ is the coordinate of atom i, and the angular brackets denote canonical averaging. Summarized in Table 1, the standard deviations show that the relative displacement grows for lighter atoms from Pb to I to MA at both 160 and 330 K. The displacements also grow with temperature, indicating that electron−vibrational interactions become stronger at 330 K. NQEs enhance atomic fluctuations. Interestingly, even fluctuations of the heavy Pb and I atoms are enhanced, most likely due to their interactions with the lighter atoms of the MA cations and the H atoms in particular. The computed standard deviations for MA are 0.606 Å (AIMD) and 0.781 Å (RPMD) at 160 K, showing a 28.9% increase due to NQEs. The corresponding increase at 330 K is much less significant, at 5.56%, from 0.953 Å (AIMD) to 1.003 Å (RPMD). The influence of NQEs is even more significant on H atoms, especially at lower temperatures. Mean square displacements (MSDs) of $MAPbI_3$ atoms, averaged over the whole system, are shown as functions of time in Figure S1 of the Supporting Information. The data further demonstrate that NQEs accelerate atomic motions compared to the classical system, particularly at lower temperatures. The larger standard deviations and time-dependent MSDs are accompanied by larger atomic fluctuations, which accelerate phonon-induced loss of electronic coherence and enhance NAC. However, NAC in HOIPs is more sensitive to structural deformation than atomic motions[60,61] because structural deformation influences charge localization. We discuss this point in the next section.

2.2. Electronic Structure. Figure 4 shows the calculated projected density of states (PDOS) of $MAPbI_3$. Each PDOS is canonically averaged over randomly selected 50 snapshots from the AIMD and RPMD trajectories at the two temperatures. The valence band maximum (VBM) is formed by 5p orbitals of I atoms and small contributions of 6s orbitals of Pb atoms. The conduction band minimum (CBM) is composed of 6p orbitals of Pb atoms. MA cations do not contribute to the

https://doi.org/10.1021/jacs.3c04412
J. Am. Chem. Soc. 2023, 145, 14112−14123

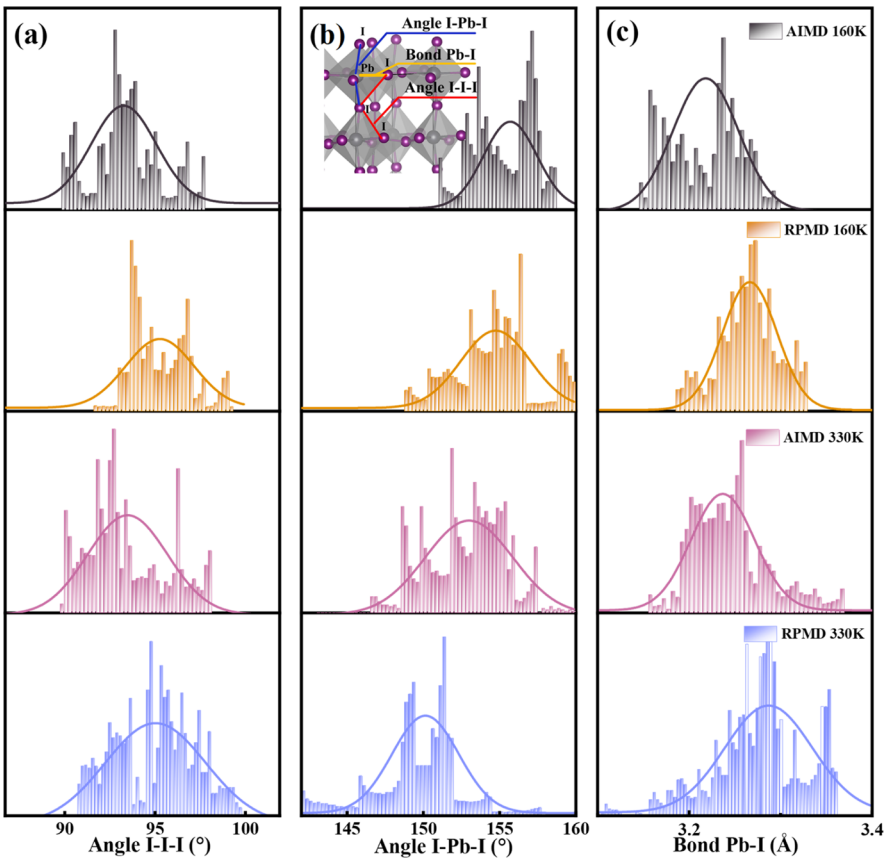

Figure 3. Distributions of the (a) I−I−I angle, (b) equatorial I−Pb−I angle, and (c) Pb−I bond length in $MAPbI_3$ during AIMD and RMPD at 160 and 330 K. The inset identifies these geometric features. The Pb−I bond length and the I−I−I angle grow with temperature, while the equatorial I−Pb−I angle decreases. The distribution becomes wider at 330 K than at 160 K, reflecting stronger geometry distortion at the higher temperature. NQEs make the distortion more pronounced.

Table 1. Standard Deviations in Positions (Å) of MA, H, Pb, and I Atoms of $MAPbI_3$ during the AIMD and RPMD Trajectories at 160 and 330 K

		MA		Pb	I
160 K	AIMD	0.606	H (0.671)	0.206	0.273
	RPMD	0.781	H (0.870)	0.309	0.390
330 K	AIMD	0.953	H (1.066)	0.390	0.434
	RPMD	1.006	H (1.149)	0.416	0.450

band edge states; however, they affect the electronic properties indirectly through steric effects, hydrogen bonding, and electrostatic interactions. The band gap decreases from 1.71 eV (Figure 4a) to 1.61 eV (Figure 4c) in the presence of NQEs at 160 K. The change is less significant at 330 K from 1.72 eV (AIMD, Figure 4b) to 1.69 eV (RPMD, Figure 4d). A smaller band gap favors a larger NAC because the NAC is inversely proportional to the energy gap.[47,54,67−69]

The NAC is governed by the overlap of the initial and final electronic states. In this regard, we computed the evolution of the inverse reference ratio (IPR) of the Kohn−Sham orbitals corresponding to the VBM and CBM, according to eq 1

$$\mathrm{IPR} = N \cdot \frac{\sum k_j^2}{\left(\sum k_j^2\right)^2} \qquad \mathrm{IPR} \in (0,1] \tag{1}$$

where N denotes the number of grid points, and k_j is the charge density corresponding to grid point j. The IPR value is used to characterize the degree of change localization. The larger the IPR value, the more localized the charge density is. IPR = 1 indicates that the charge is completely localized. Figure 5 shows the evolution of IPRs of the VBM and CBM obtained from the 3 ps AIMD and RPMD trajectories. The canonically averaged IPR values shown in the panels are larger for the VBM than the CBM, indicating that the VBM is more localized. This is likely because I atoms, supporting the VBM, are lighter than Pb atoms forming the CBM, Figure 4, undergo larger thermal fluctuations, and form a less ordered sublattice. The conclusion holds regardless of NQEs and temperature. Because the VBM is more sensitive to disorder induced by temperature and NQEs, and determines primarily the disorder-driven changes in the electronic properties and electron−vibrational interactions, we analyze the IPR of the VBM in more detail. The IPR value increases from 0.0131 (AIMD) to 0.0359 (RPMD) at 160 K, a large 174.1% change. The corresponding increase is only 43.2% at 330 K from 0.0280 (AIMD) to 0.0401 (RPMD). These IRP values lead to the following four conclusions: (1) NQEs have much more influence on charge localization at lower than at higher temperatures. (2) Temperature growth enhances charge localization. (3) NQEs have a stronger influence on charge localization than temperature increase. (4) Stronger charge localization due to NQEs and temperature leads to a smaller NAC; consider the data in Table 2: 1.51 meV (AIMD 160 K) > 1.22 meV (AIMD 330 K) > 1.02 meV (RPMD 160 K) > 0.96 meV (RPMD 330 K).

https://doi.org/10.1021/jacs.3c04412
J. Am. Chem. Soc. 2023, 145, 14112−14123

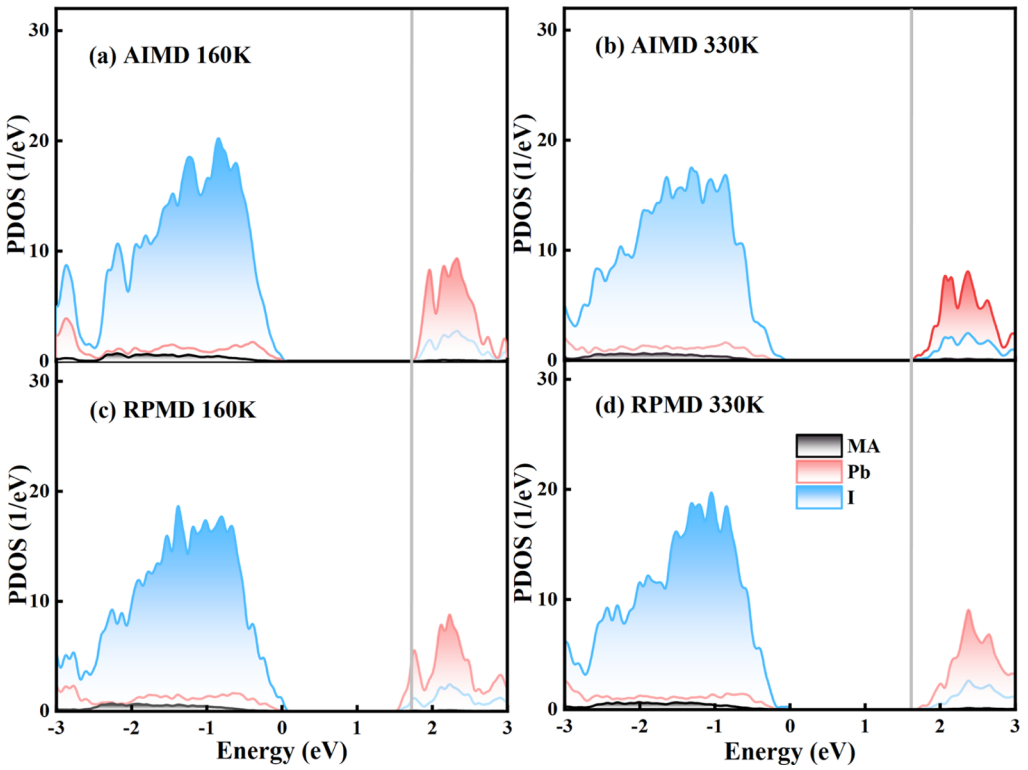

Figure 4. Canonically averaged PDOS of $MAPbI_3$ obtained using (a) AIMD at 160 K, (b) AIMD at 330 K, (c) RPMD at 160 K, and (d) RPMD at 330 K. The zero of energy is set to the VBM. The solid gray line identifies the CBM for AIMD and highlights the difference from RPMD. The AIMD band gap has little temperature dependence. However, the RPMD band gap is notably smaller at lower temperatures, emphasizing the importance of NQEs.

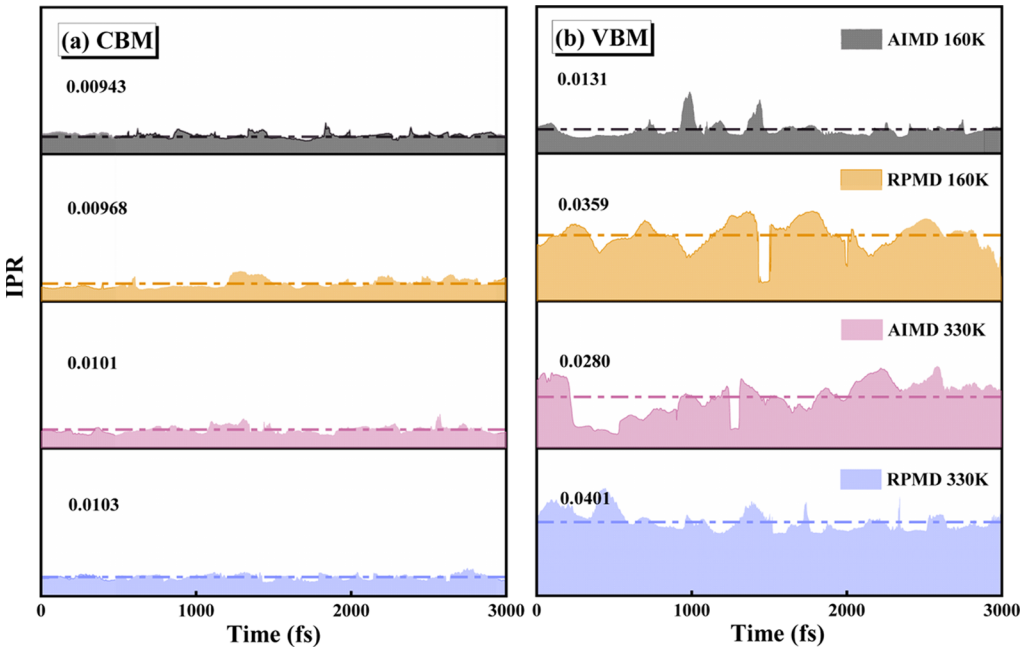

Figure 5. Evolution of the inverse participation ratio (IPR) for (a) CBM and (b) VBM of $MAPbI_3$ during the AIMD and RPMD simulations at 160 and 330 K. A higher IPR value indicates a greater degree of charge localization. The *y*-axis scale is the same in all cases. Holes (VBM) are more localized than electrons (CBM) because holes are supported by lighter I atoms, while electrons are supported by heavier Pb atoms, and lighter atoms exhibit larger fluctuations and more disorder. NQEs enhance charge localization, and their role is much more significant at the low temperature. NQEs have more influence on hole localization than temperature, cf. the top three panels in part (b).

Figure 6 shows the evolution of the overlap of the VBM and CBM charge densities. A larger overlap should favor a stronger NAC. The electron−hole overlap is smaller in the presence of NQEs at both temperatures, indicating once again that NQEs induce additional disorder and charge localization. The electron−hole overlap decreases in the series 0.00410

https://doi.org/10.1021/jacs.3c04412
J. Am. Chem. Soc. 2023, 145, 14112−14123

Table 2. Canonically Averaged Band Gap, Absolute NAC, Pure-Dephasing Time, and Nonradiative and Radiative Recombination Times for the VBM−CBM Transition of $MAPbI_3$ Obtained Using AIMD and RPMD at 160 and 330 K

		bandgap (eV)	NAC (meV)	dephasing (fs)	nonradiative recombination (ns)	radiative recombination (ns)
160 K	AIMD	1.71	1.51	11.57	0.95	2.57
	RPMD	1.61	1.02	6.63	2.57	3.57
330 K	AIMD	1.72	1.22	8.34	2.16	2.83
	RPMD	1.69	0.96	5.88	2.92	3.99

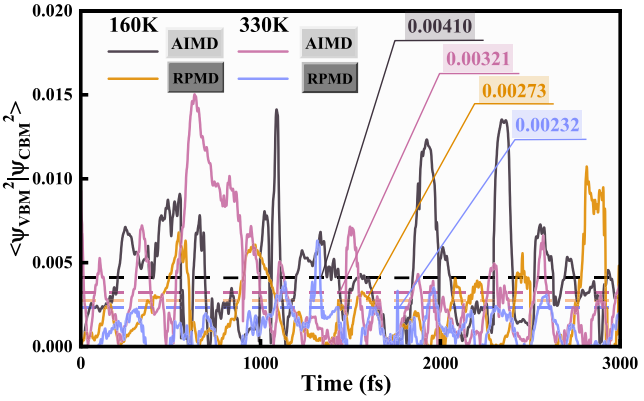

Figure 6. Evolution of overlap of the VBM and CBM charge densities in $MAPbI_3$ for the AIMD and RPMD simulations at 160 and 330 K. Electrons and holes become more separated at the higher temperature, and their overlap decreases, as demonstrated by the dashed lines showing the average overlaps. The electron−hole overlap is smaller when NQEs are included.

(AIMD 160 K) > 0.00321 (AIMD 330 K) > 0.00273 (RPMD 160 K) > 0.00232 (RPMD 330 K), which correlates with the NAC values reported in Table 2. Smaller NACs can reduce the nonradiative electron−hole recombination and prolong the charge carrier lifetime.

2.3. Electron−Vibrational Interaction. Electron−vibrational interactions give rise to elastic and inelastic electron−phonon scattering. Inelastic scattering allows the energy to be converted from electrons to phonons, while elastic electron−phonon scattering disrupts coherence between electronic states. The two types of scattering are related. For example, by destroying coherence, elastic processes slow down nonradiative relaxation that occurs via inelastic scattering, as exemplified by the quantum Zeno effect.[70−73] The frequencies of the vibrational motions that couple to the electronic subsystem during a nonadiabatic transitions can be identified by Fourier transform of the phonon-driven fluctuation of the electronic energy gap. FT of the autocorrelation function (ACF) of the energy gap fluctuation is known as the spectral density. Spectral densities for the band gap transition obtained using AIMD and RPMD at 160 and 330 K are shown in Figure 7a. FTs of the ACF of the difference of the IPRs of the CBM and VBM are presented in Figure 7b, while FTs of the ACF of the overlap of the CBM and VBM charge densities are shown in Figure 7c. The strongest signals are seen at low-frequencies, corresponding to Pb−I bending near 62−70 cm^{-1},[74] Pb−I stretching at around 100 cm^{-1},[75] and other low-frequency vibrations of the Pb−I in the organic lattice. Weaker but still significant signals are seen above 100 cm^{-1}, including Raman active motions of the organic cations at 120−180 cm^{-1}.[75] The signals above 200 cm^{-1} are related to C−N torsion.[76,77] Unlike the direct contribution of motions of the Pb−I framework to the NAC, organic cations have an indirect effect on the electron−hole recombination through electrostatic interactions and perturbation of the inorganic lattice.[24−26] As temperature increases, the intensity of the low-frequency peaks grows, and new vibrational signals in the higher-frequency region appear. NQEs enhance the motion of MA cations, intensifying the peaks in the high-frequency region.

The pure-dephasing function characterizing elastic electron−vibrational scattering can be calculated using the second-order cumulant approximation of the optical response theory.[78−82]

$$D_{ij}(t) = \exp\left\{-\frac{1}{\hbar^2}\int_0^t dt' \int_0^{t'} dt'' C_{ij}(t'')\right\} \quad (2)$$

here, $C_{ij}(t)$ is the unnormalized ACF of the CBM−VBM energy gap. The pure-dephasing functions and ACF are shown in Figure 8. The pure-dephasing functions of Figure 8a are fitted by Gaussians $\exp[0.5(-t/\tau)^2]$ to obtain the decoherence

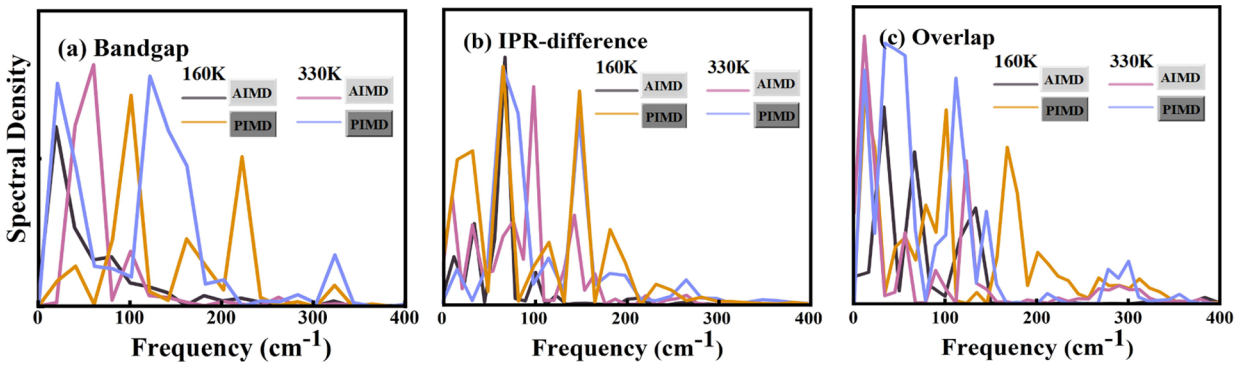

Figure 7. Spectral densities obtained by Fourier transforms of the ACF of (a) VBM−CBM band gap fluctuations, (b) VBM−CBM IPR difference, and (c) overlap of electron and hole charge densities for $MAPbI_3$ obtained using AIMD and RPMD at 160 and 330 K. Low-frequency vibrations dominate the electron−phonon coupling and nonradiative electron−hole recombination. Higher-frequency modes become more active at higher temperatures and in the presence of NQEs.

https://doi.org/10.1021/jacs.3c04412
J. Am. Chem. Soc. 2023, 145, 14112−14123

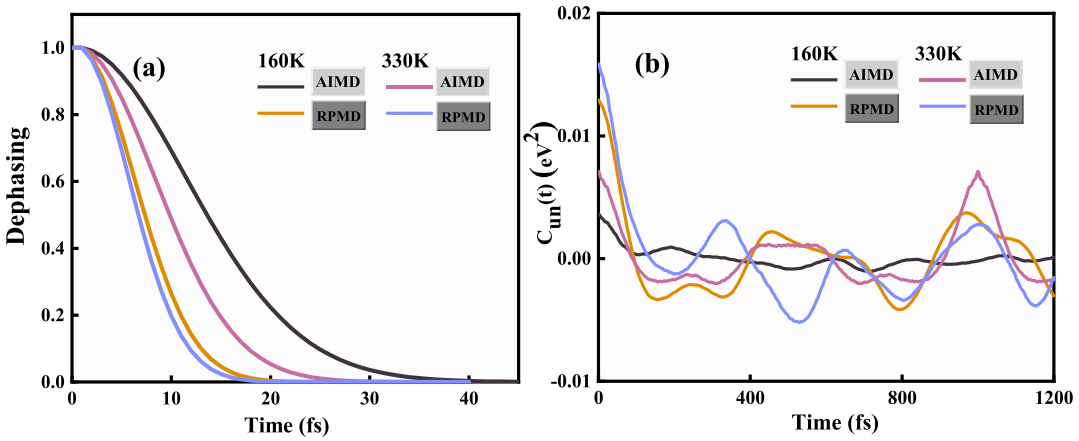

Figure 8. (a) Pure-dephasing functions for the VBM−CBM transition, and (b) unnormalized ACFs of the VBM−CBM band gap fluctuation in $MAPbI_3$ for the AIMD and RPMD simulations at 160 and 330 K. The ACF initial value equals the square of the band gap fluctuation. A larger initial value leads to a shorter pure-dephasing time.

times reported in Table 2. Both increased temperature and NQEs accelerate decoherence, c.f., AIMD 160 K (11.57 fs), RPMD 160 K (6.63 fs), AIMD 330 K (8.34 fs), and RPMD 330 K (5.88 fs). Similarly to the other properties discussed above, the coherence time changes more due to NQEs at lower temperatures than at higher temperatures. The decoherence rate is closely related to the initial value of the unnormalized ACF, representing energy gap fluctuation,[79] Figure 8b. The ACF initial values are AIMD 160 K (0.00364 eV^2), RPMD 160 K (0.01293 eV^2), AIMD 330 K (0.00711 eV^2), and RPMD 330 K (0.01589 eV^2), showing the expected correlation with the decoherence rate. Typically, faster decoherence favors a longer carrier lifetime.

2.4. Electron−Hole Recombination. Figure 9 shows the nonradiative decay of the population of the first excited state (CBM) in the systems under investigation obtained by NA-MD coupled to AIMD and RPMD. Fitting the data using an exponential decay $P(t) = \exp\left(-\frac{t}{\tau}\right)$ gives the recombination time, τ, reported in Table 2. The obtained few nanosecond nonradiative recombination times are consistent with the experimental measurements.[83−86] The nonradiative electron−hole recombination time increases with temperature and upon incorporation of NQEs: AIMD 160 K (0.95 ns), RPMD 160 K (2.57 ns), AIMD 330 K (2.16 ns), and RPMD 330 K (2.92 ns). The increase of the carrier lifetime with temperature is an unusual and important feature of HOIPs observed experimentally[87−90] and rationalized theoretically by increased disorder that partially localizes electrons and holes and reduces their interaction.[60,61,66,91,92] Interestingly, NQEs increase the lifetime at both 160 and 330 K temperatures. The increase is greater at lower temperatures, with the RPMD lifetime extended by 170.5% compared to the AIMD lifetime. The corresponding enhancement at 330 K is 35.2%.

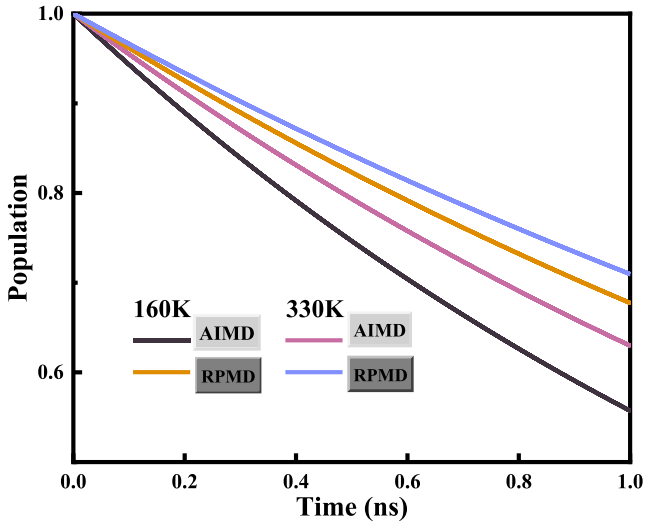

Figure 9. Nonradiative electron−hole recombination dynamics in $MAPbI_3$ obtained using NA-MD coupled to AIMD and RPMD at 160 and 330 K. NQEs slow down the recombination by creating an additional disorder that decreases the NAC and shortens the decoherence time, particularly at lower temperatures.

The average radiative lifetimes were also calculated based on the Einstein coefficient of spontaneous emission, eq S3 of the Supporting Information and reported in Table 2, Figure S2 shows distributions of the radiative lifetimes. The radiative lifetimes calculated for the current systems are a few nanoseconds and are comparable to the nonradiative lifetimes, indicating that both radiative and nonradiative decay channels contribute to charge carrier losses. Similarly to the nonradiative timescales, the radiative lifetimes are extended after the incorporation of NQEs due to increased disorder and reduced electron−hole overlap. NQEs also make the distributions of the radiative lifetimes broader, Figure S2. Interestingly, the influence of NQEs on the radiative lifetimes is comparable at lower and higher temperatures, while NQEs have a more significant influence on the nonradiative lifetimes at the lower temperature, Table 2. This is because nonradiative lifetimes depend on structural disorder and atomic velocities, both of which are enhanced by NQEs. In comparison, radiative lifetimes depend only on structure.

Combining the above factors, we can rationalize the difference in the nonradiative and radiative electron−hole recombination times in the presence and absence of NQEs at different temperatures. The main factors affecting the dynamics are the structure that influences charge localization, the band gap that enters the lifetime expressions, the transition dipole moment that depends on the electron−hole overlap, NAC that is influenced by both electron−hole overlap and atomic motions, and decoherence time that depends on phonon-

https://doi.org/10.1021/jacs.3c04412
J. Am. Chem. Soc. 2023, 145, 14112−14123

driven fluctuations of the band gap. The structural disorder enhanced by both NQEs and temperature is the key factor rationalizing the observed trends. The disorder localizes the charges, especially holes, reduces electron−hole overlap, and as a result, decreases both the optical transition dipole moment and NAC. Both NQEs and temperature influence the band gap; however, the changes in the band gap are relatively minor. Atomic motions are enhanced by NQEs, and this should increase the NAC. However, the NAC is determined by electron and hole wavefunctions that are localized on the Pb−I inorganic framework. Pb and I atoms are heavy, and their motions are influenced little by NQE. Motions of the light H atoms of the MA species are influenced strongly by NQEs; however, H atoms influence the NAC only indirectly by modifying the structural dynamics of the Pb−I lattice and through long-range electrostatic interactions with the charges. The coherence times are shortened by NQEs because of enhanced phonon-induced band gap fluctuations. Shorter coherence times generally favor longer excited state lifetimes. It is interesting to note that elastic electron−vibrational interactions are enhanced by NQEs, as evidenced by shorter coherence times. At the same time, inelastic electron−vibrational scattering is slowed down by NQEs. Although atomic motions are enhanced, charges are more localized due to disorder, and overall, NAC matrix elements are reduced. The influence of NQEs on electron−vibrational processes is more significant at lower temperatures, while the influence of NQEs on radiative processes is weakly temperature dependent. The reported detailed atomistic analysis indicates that NQEs have a notable influence on charge carrier dynamics in HOIPs, despite the fact that charge carriers are supported by heavy Pb and I atoms. This is yet another unusual feature of these very interesting materials.

3. CONCLUSIONS

By combining NA-MD simulations with classical, AIMD, quantum path integral, RPMD, treatments of atomic motions, we have demonstrated that NQEs have a significant influence on charge carrier lifetimes in HOIPs, making both nonradiative and radiative lifetimes longer. The influence arises largely from the enhanced structural fluctuations and disorder due to NQEs, the resulting additional localization of charge carriers, especially holes, and reduced electron−hole interactions. The conclusion holds at both low and ambient temperatures and has important implications for device performance. On the one hand, extended carrier lifetimes can improve the efficiency of solar energy and other optoelectronic devices because they reduce charge carrier losses. On the other hand, enhanced localization can deteriorate charge transport.

The fact that the charge carrier dynamics is influenced by NQEs is surprising because the carriers are supported by heavy Pb and I atoms of the HOIP inorganic framework. NQEs act indirectly by enhancing motions of the light atoms of the organic MA species and, in particular, H atoms, which in turn, influence the dynamics of the inorganic lattice, enhancing the overall disorder. This mechanism also rationalizes the facts that NQEs have influence at both low and ambient temperatures, and that both nonradiative and radiative lifetimes are affected, even though the radiative lifetime does not depend on atomic motion. Typically, NQEs are expected to be significant only at low temperatures for light atoms and for processes that depend on atomic motion. In HOIPs, the light atoms couple structurally to the heavy atoms, and structure influences all electronic properties, including the band gap and the optical transition dipole moment, in addition to the electron−vibrational interactions. The influence of NQEs on most properties is more significant at lower temperatures. At 160 K, the band gap is reduced by 0.10 eV, and the nonradiative lifetime is enhanced by a factor of 3. At 330 K, the band gap is reduced by 0.03 eV, and the nonradiative lifetime is enhanced by 1/3. NQEs increase the radiative lifetime by 40% at both temperatures and make the lifetime distributions twice as broader. The distribution of the structural features, such as the I−I−I angle between $[PbI_6]^{4-}$ octahedra and the I−Pb−I angle characterizing the $[PbI_6]^{4-}$ octahedron shape, is generally broadened by NQEs. The Pb−I bond lengthens by 0.1 Å. NQEs introduce new, higher frequency vibrations that couple to the electronic subsystem. Electronic coherence times are consistently shorter in the presence of NQEs at all temperatures. Interestingly, NQEs have opposite influences on elastic (coherence) and inelastic (NAC) electron−vibrational scattering in the present case. The influence of NQEs on the elastic scattering is dominated by the enhanced phonon-driven fluctuations of the band gap, while the inelastic electron−hole recombination is governed by charge localization and overlap. The influence of NQEs on the charge carrier dynamics is similar to that of an increased temperature; however, a straightforward temperature increase cannot fully model NQEs in mixed atom systems because NQEs and temperature effects have different dependences on atomic mass.

The reported detailed atomistic analysis provides another important insight into the unusual properties of HOIPs, contributing to the fundamental knowledge that guides the development of novel optoelectronic materials.

4. COMPUTATIONAL METHODS

The geometry optimization, electronic structure, AIMD, and NAC calculations were performed using the Vienna ab initio simulation package (VASP).[93] The RPMD was conducted by combining VASP with the I-PI software to include NQEs.[94,95] The Perdew−Burke−Ernzerhof functional[96] was used to handle electron exchange−correlation interactions, while the interactions between the ionic core and valence electrons were treated by the projector-augmented wave (PAW) method.[97] The van der Waals interactions were treated using the Grimme-D3 method.[98] The plane wave energy cutoff was set to 500 eV, and the geometry was optimized using a 3 × 3 × 3 Monkhorst−Pack *k*-point grid.[99] The convergence accuracy of the force was set to 0.01 eV/Å. A denser 4 × 4 × 4 *k*-point grid was used to calculate the density of states.

After geometry optimization, the systems were heated to 160 K and then 330 K for 2 ps by velocity rescaling. After that, 10 ps AIMD was run in the microcanonical ensemble at 160 and 330 K with a 0.5 fs atomic time step to achieve full equilibration. Subsequently, 3 ps production trajectories were generated in the microcanonical ensemble for the systems prepared at 160 and 330 K. Similarly, 3 ps RPMD trajectories were simulated in the microcanonical ensemble[100,101] using 16 beads, as justified by the total energy convergence test (Figure S3). The 3 ps AIMD and RPMD production runs were used to calculate the NAC between the VBM and CBM at the Γ-point because tetragonal $MAPbI_3$ possesses a direct band gap at the Γ-point. Note that NAC depends on derivatives of electronic wavefunctions with respect to atomic positions.[102,103] Computing the derivatives for each bead and averaging them over beads does not produce a reliable NAC. Instead, the center-of-mass trajectory of the beads was used to compute the NAC in RPMD. The other electronic properties, such as KS orbital energies, were calculated by averaging them over the beads.[42] 3000 geometries were chosen from the production runs every 1 fs and were used as initial conditions for the

https://doi.org/10.1021/jacs.3c04412
J. Am. Chem. Soc. 2023, 145, 14112−14123

NA-MD simulations. The NA-MD simulations were performed using the PYthon eXtension for Ab Initio Dynamics (PYXAID) code.[69,104]

The NA-MD simulations[54] were performed using the decoherence-induced surface hopping (DISH)[105] technique implemented in TD-DFT based on the Kohn−Sham (KS) framework.[106,107] Decoherence is the destruction of the superposition state formed by a pair of electronic states in the system via NAC.[104,105] The decoherence time can be estimated as the pure-dephasing time in optical response theory.[78] In the DISH algorithm, quantum jumps occur as a result of the decoherence process, which provides the physical basis for the jumps.[104,105,108] This method has been applied to study the photoexcitation dynamics of various materials, including metal oxides,[109−112] low-dimensional materials,[113−116] perovskites,[23,25,27,28,117−120] and other systems.[121,122]

■ ASSOCIATED CONTENT

Supporting Information

The Supporting Information is available free of charge at https://pubs.acs.org/doi/10.1021/jacs.3c04412.

Summary of RPMD, dependence of the total energy on the number of beads, evolution of mean-square displacements of atoms, and distributions of radiative lifetimes in MAPbI3 for AIMD and RPMD at 160 and 330 K (PDF)

■ AUTHOR INFORMATION

Corresponding Author

Run Long − *College of Chemistry, Key Laboratory of Theoretical & Computational Photochemistry of Ministry of Education, Beijing Normal University, Beijing 100875, P. R. China;* orcid.org/0000-0003-3912-8899; Email: runlong@bnu.edu.cn

Authors

Yulong Liu − *College of Chemistry, Key Laboratory of Theoretical & Computational Photochemistry of Ministry of Education, Beijing Normal University, Beijing 100875, P. R. China*

Wei-Hai Fang − *College of Chemistry, Key Laboratory of Theoretical & Computational Photochemistry of Ministry of Education, Beijing Normal University, Beijing 100875, P. R. China;* orcid.org/0000-0002-1668-465X

Oleg V. Prezhdo − *Departments of Chemistry, and Physics and Astronomy, University of Southern California, Los Angeles, California 90089, United States;* orcid.org/0000-0002-5140-7500

Complete contact information is available at: https://pubs.acs.org/10.1021/jacs.3c04412

Notes

The authors declare no competing financial interest.

■ ACKNOWLEDGMENTS

This work was supported by the Beijing Natural Science Foundation (grant no. 2212031) and the National Natural Science Foundation of China (grant nos. 21973006 and 22288201). R.L. acknowledges the Beijing Normal University Startup Package. O.V.P. acknowledges the support of the US National Science Foundation (grant CHE-2154367).

■ REFERENCES

(1) Prasanna, R.; Gold-Parker, A.; Leijtens, T.; Conings, B.; Babayigit, A.; Boyen, H. G.; Toney, M. F.; McGehee, M. D. Band Gap Tuning via Lattice Contraction and Octahedral Tilting in Perovskite Materials for Photovoltaics. *J. Am. Chem. Soc.* **2017**, *139*, 11117−11124.

(2) Pellet, N.; Gao, P.; Gregori, G.; Yang, T. Y.; Nazeeruddin, M. K.; Maier, J.; Gratzel, M. Mixed-Organic-Cation Perovskite Photovoltaics for Enhanced Solar-Light Harvesting. *Angew. Chem., Int. Ed.* **2014**, *53*, 3151−3157.

(3) Meggiolaro, D.; Motti, S. G.; Mosconi, E.; Barker, A. J.; Ball, J.; Andrea Riccardo Perini, C.; Deschler, F.; Petrozza, A.; De Angelis, F. Iodine Chemistry Determines the Defect Tolerance of Lead-Halide Perovskites. *Energy Environ. Sci.* **2018**, *11*, 702−713.

(4) Lian, Z. P.; Yan, Q. F.; Gao, T. T.; Ding, J.; Lv, Q. R.; Ning, C. G.; Li, Q.; Sun, J. L. Perovskite $CH_3NH_3PbI_3$(Cl) Single Crystals: Rapid Solution Growth, Unparalleled Crystalline Quality, and Low Trap Density toward 10^8 cm^{-3}. *J. Am. Chem. Soc.* **2016**, *138*, 9409−9412.

(5) Yang, W. S.; Noh, J. H.; Jeon, N. J.; Kim, Y. C.; Ryu, S.; Seo, J.; Seok, S. I. High-Performance Photovoltaic Perovskite Layers Fabricated Through Intramolecular Exchange. *Science* **2015**, *348*, 1234−1237.

(6) Zhang, F.; Kim, D. H.; Lu, H. P.; Park, J. S.; Larson, B. W.; Hu, J.; Gao, L. G.; Xiao, C. X.; Reid, O. G.; Chen, X. H.; Zhao, Q.; Ndione, P. F.; Berry, J. J.; You, W.; Walsh, A.; Beard, M. C.; Zhu, K. Enhanced Charge Transport in 2D Perovskites via Fluorination of Organic Cation. *J. Am. Chem. Soc.* **2019**, *141*, 5972−5979.

(7) Scajev, P.; Qin, C.; Aleksiejūnas, R.; Baronas, P.; Miasojedovas, S.; Fujihara, T.; Matsushima, T.; Adachi, C.; Jursenas, S. Diffusion Enhancement in Highly Excited $MAPbI_3$ Perovskite Layers with Additives. *J. Phys. Chem. Lett.* **2018**, *9*, 3167−3172.

(8) Arias, D. H.; Moore, D. T.; van de Lagemaat, J.; Johnson, J. C. Direct Measurements of Carrier Transport in Polycrystalline Methylammonium Lead Iodide Perovskite Films with Transient Grating Spectroscopy. *J. Phys. Chem. Lett.* **2018**, *9*, 5710−5717.

(9) Wehrenfennig, C.; Eperon, G. E.; Johnston, M. B.; Snaith, H. J.; Herz, L. M. High Charge Carrier Mobilities and Lifetimes in Organolead Trihalide Perovskites. *Adv. Mater.* **2014**, *26*, 1584−1589.

(10) Kojima, A.; Teshima, K.; Shirai, Y.; Miyasaka, T. Organometal Halide Perovskites as Visible-Light Sensitizers for Photovoltaic Cells. *J. Am. Chem. Soc.* **2009**, *131*, 6050−6051.

(11) Kim, M.; Jeong, J.; Lu, H. Z.; Lee, T. K.; Eickemeyer, F. T.; Liu, Y. H.; Choi, I. W.; Choi, S. J.; Jo, Y.; Kim, H. B.; Mo, S. I.; Kim, Y. K.; Lee, H.; An, N. G.; Cho, S.; Tress, W. R.; Zakeeruddin, S. M.; Hagfeldt, A.; Kim, J. Y.; Gratzel, M.; Kim, D. S. Conformal Quantum Dot-SnO_2 Layers as Electron Transporters for Efficient Perovskite Solar Cells. *Science* **2022**, *375*, 302−306.

(12) Li, Y. J.; Lv, Y. C.; Zou, C. L.; Zhang, W.; Yao, J. N.; Zhao, Y. S. Output Coupling of Perovskite Lasers from Embedded Nanoscale Plasmonic Waveguides. *J. Am. Chem. Soc.* **2016**, *138*, 2122−2125.

(13) Cao, F. R.; Meng, L. X.; Wang, M.; Tian, W.; Li, L. Gradient Energy Band Driven High-Performance Self-Powered Perovskite/CdS Photodetector. *Adv. Mater.* **2019**, *31*, 1806725.

(14) Shoaib, M.; Zhang, X. H.; Wang, X. X.; Zhou, H.; Xu, T.; Wang, X.; Hu, X. L.; Liu, H. W.; Fan, X. P.; Zheng, W. H.; Yang, T. F.; Yang, S. Z.; Zhang, Q. L.; Zhu, X. L.; Sun, L. T.; Pan, A. L. Directional Growth of Ultralong $CsPbBr_3$ Perovskite Nanowires for High-Performance Photodetectors. *J. Am. Chem. Soc.* **2017**, *139*, 15592−15595.

(15) Liu, Y.; Dong, Y. T.; Zhu, T.; Ma, D. X.; Proppe, A.; Chen, B.; Zheng, C.; Hou, Y.; Lee, S. J.; Sun, B.; Jung, E. H.; Yuan, F. L.; Wang, Y. K.; Sagar, L. K.; Hoogland, S.; García de Arquer, F. P.; Choi, M. J.; Singh, K.; Kelley, S. O.; Voznyy, O.; Lu, Z. H.; Sargent, E. H. Bright and Stable Light-Emitting Diodes Based on Perovskite Quantum Dots in Perovskite Matrix. *J. Am. Chem. Soc.* **2021**, *143*, 15606−15615.

(16) Wei, Z. H.; Xing, J. The Rise of Perovskite Light-Emitting Diodes. *J. Phys. Chem. Lett.* **2019**, *10*, 3035−3042.

(17) Wu, Y. X.; Li, J.; Xu, J.; Du, Y. Y.; Huang, L. K.; Ni, J.; Cai, H. K.; Zhang, J. J. Organic-Inorganic Hybrid $CH_3NH_3PbI_3$ Perovskite Materials as Channels in Thin-Film Field-Effect Transistors. *RSC Adv.* **2016**, *6*, 16243−16249.

(18) Jaramillo-Quintero, O. A.; Sanchez, R. S.; Rincon, M.; Mora-Sero, I. Bright Visible-Infrared Light Emitting Diodes Based on Hybrid Halide Perovskite with Spiro-OMeTAD as a Hole-Injecting Layer. *J. Phys. Chem. Lett.* **2015**, *6*, 1883−1890.
(19) Leyden, M. R.; Meng, L.; Jiang, Y.; Ono, L. K.; Qiu, L.; Juarez-Perez, E. J.; Qin, C.; Adachi, C.; Qi, Y. Methylammonium Lead Bromide Perovskite Light-Emitting Diodes by Chemical Vapor Deposition. *J. Phys. Chem. Lett.* **2017**, *8*, 3193−3198.
(20) Yakunin, S.; Protesescu, L.; Krieg, F.; Bodnarchuk, M. I.; Nedelcu, G.; Humer, M.; De Luca, G.; Fiebig, M.; Heiss, W.; Kovalenko, M. V. Low-threshold Amplified Spontaneous Emission and Lasing From Colloidal Nanocrystals of Caesium Lead Halide Perovskites. *Nat. Commun.* **2015**, *6*, 8056.
(21) Maculan, G.; Sheikh, A. D.; Abdelhady, A. L.; Saidaminov, M. I.; Haque, M. A.; Murali, B.; Alarousu, E.; Mohammed, O. F.; Wu, T.; Bakr, O. M. $CH_3NH_3PbCl_3$ Single Crystals: Inverse Temperature Crystallization and Visible-Blind UV-Photodetector. *J. Phys. Chem. Lett.* **2015**, *6*, 3781−3786.
(22) Su, J.; Zheng, Q.; Shi, Y.; Zhao, J. Interlayer Polarization Explains Slow Charge Recombination in Two-Dimensional Halide Perovskites by Nonadiabatic Molecular Dynamics Simulation. *J. Phys. Chem. Lett.* **2020**, *11*, 9032−9037.
(23) Shi, R.; Fang, Q.; Vasenko, A. S.; Long, R.; Fang, W. H.; Prezhdo, O. V. Structural Disorder in Higher-Temperature Phases Increases Charge Carrier Lifetimes in Metal Halide Perovskites. *J. Am. Chem. Soc.* **2022**, *144*, 19137−19149.
(24) Liu, Y.; Long, R.; Fang, W. H. Great Influence of Organic Cation Motion on Charge Carrier Dynamics in Metal Halide Perovskite Unraveled by Unsupervised Machine Learning. *J. Phys. Chem. Lett.* **2022**, *13*, 8537−8545.
(25) Lu, H.; Fang, W. H.; Long, R. Collective Motion Improves the Stability and Charge Carrier Lifetime of Metal Halide Perovskites: A Phonon-Resolved Nonadiabatic Molecular Dynamics Study. *J. Phys. Chem. Lett.* **2022**, *13*, 3016−3022.
(26) Zhao, X.; Lu, H.; Fang, W. H.; Long, R. Correlated Organic-Inorganic Motion Enhances Stability and Charge Carrier Lifetime in Mixed Halide Perovskites. *Nanoscale* **2022**, *14*, 4644−4653.
(27) Lu, H.; Long, R. Spin-Orbit Coupling Notably Retards Non-radiative Electron-Hole Recombination in Methylammonium Lead Triiodide Perovskites. *J. Phys. Chem. Lett.* **2023**, *14*, 2715−2721.
(28) Shi, R.; Long, R. Atomic Model for Alkali Metal-Doped Tin-Lead Mixed Perovskites: Insight from Quantum Dynamics. *J. Phys. Chem. Lett.* **2023**, *14*, 2878−2885.
(29) Shi, R.; Fang, W. H.; Vasenko, A. S.; Long, R.; Prezhdo, O. V. Efficient Passivation of DY Center in $CH_3NH_3PbBr_3$ by Chlorine: Quantum Molecular Dynamics. *Nano Res.* **2022**, *15*, 2112−2122.
(30) Liu, D. Y.; Perez, C. M.; Vasenko, A. S.; Prezhdo, O. V. Ag-Bi Charge Redistribution Creates Deep Traps in Defective $Cs_2AgBiBr_6$: Machine Learning Analysis of Density Functional Theory. *J. Phys. Chem. Lett.* **2022**, *13*, 3645−3651.
(31) Liu, D.; Wu, Y.; Vasenko, A. S.; Prezhdo, O. V. Grain Boundary Sliding and Distortion on a Nanosecond Timescale Induce Trap States in $CsPbBr_3$: Ab Initio Investigation with Machine Learning Force Field. *Nanoscale* **2023**, *15*, 285−293.
(32) Markland, T. E.; Ceriotti, M. Nuclear Quantum Effects Enter the Mainstream. *Nat. Rev. Chem.* **2018**, *2*, 0109.
(33) Habershon, S.; Manolopoulos, D. E.; Markland, T. E.; Miller, T. F., III Ring-Polymer Molecular Dynamics: Quantum Effects in Chemical Dynamics from Classical Trajectories in an Extended Phase Space. *Annu. Rev. Phys. Chem.* **2013**, *64*, 387−413.
(34) Craig, I. R.; Manolopoulos, D. E. Quantum Statistics and Classical Mechanics: Real Time Correlation Functions from Ring Polymer Molecular Dynamics. *J. Chem. Phys.* **2004**, *121*, 3368−3373.
(35) Li, X.-Z.; Walker, B.; Michaelides, A. Quantum Nature of the Hydrogen Bond. *Proc. Natl. Acad. Sci. U.S.A.* **2011**, *108*, 6369−6373.
(36) Fang, W.; Chen, J.; Feng, Y.; Li, X.-Z.; Michaelides, A. The Quantum Nature of Hydrogen. *Int. Rev. Phys. Chem.* **2019**, *38*, 35−61.
(37) Marx, D.; Tuckerman, M. E.; Hutter, J.; Parrinello, M. The Nature of the Hydrated Excess Proton in Water. *Nature* **1999**, *397*, 601−604.
(38) Gao, J. L.; Truhlar, D. G. Quantum Mechanical Methods for Enzyme Kinetics. *Annu. Rev. Phys. Chem.* **2002**, *53*, 467−505.
(39) Chmiela, S.; Sauceda, H. E.; Poltavsky, I.; Muller, K. R.; Tkatchenko, A. SGDML: Constructing Accurate and Data Efficient Molecular Force Fields Using Machine Learning. *Comput. Phys. Commun.* **2019**, *240*, 38−45.
(40) Zhou, W. H.; Mandal, A.; Huo, P. F. Quasi-Diabatic Scheme for Nonadiabatic On-the-Fly Simulations. *J. Phys. Chem. Lett.* **2019**, *10*, 7062−7070.
(41) Kundu, A.; Song, Y. X.; Galli, G. Influence of Nuclear Quantum Effects on the Electronic Properties of Amorphous Carbon. *Proc. Natl. Acad. Sci. U.S.A.* **2022**, *119*, No. e2203083119.
(42) Chu, W. B.; Tan, S. J.; Zheng, Q. J.; Fang, W.; Feng, Y. X.; Prezhdo, O. V.; Wang, B.; Li, X. Z.; Zhao, J. Ultrafast Charge Transfer Coupled to Quantum Proton Motion at Molecule/Metal Oxide Interface. *Sci. Adv.* **2022**, *8*, No. eabo2675.
(43) Prezhdo, O. V. Classical Mapping for Second-Order Quantized Hamiltonian Dynamics. *J. Chem. Phys.* **2002**, *117*, 2995−3002.
(44) Prezhdo, O. V. Quantized Hamilton Dynamics. *Theor. Chem. Acc.* **2006**, *116*, 206−218.
(45) Vaillant, C. L.; Wales, D. J.; Althorpe, S. C. Tunneling Splittings in Water Clusters from Path Integral Molecular Dynamics. *J. Phys. Chem. Lett.* **2019**, *10*, 7300−7304.
(46) Amat, A.; Mosconi, E.; Ronca, E.; Quarti, C.; Umari, P.; Nazeeruddin, M. K.; Gratzel, M.; De Angelis, F. Cation-Induced Band-Gap Tuning in Organohalide Perovskites: Interplay of Spin-Orbit Coupling and Octahedra Tilting. *Nano Lett.* **2014**, *14*, 3608−3616.
(47) Worth, G. A.; Cederbaum, L. S. Beyond Born-Oppenheimer: Molecular Dynamics Through a Conical Intersection. *Annu. Rev. Phys. Chem.* **2004**, *55*, 127−158.
(48) Barbatti, M. Nonadiabatic Dynamics with Trajectory Surface Hopping Method. *Wiley Interdiscip. Rev.: Comput. Mol. Sci.* **2011**, *1*, 620−633.
(49) Curchod, B. F. E.; Martinez, T. J. Ab Initio Nonadiabatic Quantum Molecular Dynamics. *Chem. Rev.* **2018**, *118*, 3305−3336.
(50) Tully, J. C. Perspective: Nonadiabatic Dynamics Theory. *J. Chem. Phys.* **2012**, *137*, 22A301.
(51) Worth, G. A.; Meyer, H. D.; Koppel, H.; Cederbaum, L. S.; Burghardt, I. Using the MCTDH Wavepacket Propagation Method to Describe Multimode Non-Adiabatic Dynamics. *Int. Rev. Phys. Chem.* **2008**, *27*, 569−606.
(52) Richter, M.; Marquetand, P.; Gonzalez-Vazquez, J.; Sola, I.; Gonzalez, L. SHARC: Ab Initio Molecular Dynamics with Surface Hopping in the Adiabatic Representation Including Arbitrary Couplings. *J. Chem. Theory Comput.* **2011**, *7*, 1253−1258.
(53) Wang, L. J.; Akimov, A.; Prezhdo, O. V. Recent Progress in Surface Hopping: 2011-2015. *J. Phys. Chem. Lett.* **2016**, *7*, 2100−2112.
(54) Prezhdo, O. V. Modeling Non-Adiabatic Dynamics in Nanoscale and Condensed Matter Systems. *Acc. Chem. Res.* **2021**, *54*, 4239−4249.
(55) Runge, E.; Gross, E. K. U. Density-Functional Theory for Time-Dependent Systems. *Phys. Rev. Lett.* **1984**, *52*, 997−1000.
(56) Marques, M. A. L.; Gross, E. K. U. Time-Dependent Density Functional Theory. *Annu. Rev. Phys. Chem.* **2004**, *55*, 427−455.
(57) Brivio, F.; Frost, J. M.; Skelton, J. M.; Jackson, A. J.; Weber, O. J.; Weller, M. T.; Goni, A. R.; Leguy, A. M. A.; Barnes, P. R. F.; Walsh, A. Lattice Dynamics and Vibrational Spectra of the Orthorhombic, Tetragonal, and Cubic Phases of Methylammonium Lead Iodide. *Phys. Rev. B: Condens. Matter Mater. Phys.* **2015**, *92*, 144308.
(58) Tantardini, C.; Kokott, S.; Gonze, X.; Levchenko, S. V.; Saidi, W. A. Self-trapping" in Solar Cell Hybrid Inorganic-Organic Perovskite Absorbers. *Appl. Mater. Today* **2022**, *26*, 101380.

https://doi.org/10.1021/jacs.3c04412
J. Am. Chem. Soc. 2023, 145, 14112−14123

(59) Thind, A. S.; Huang, X.; Sun, J. W.; Mishra, R. First-Principles Prediction of a Stable Hexagonal Phase of $CH_3NH_3PbI_3$. *Chem. Mater.* **2017**, *29*, 6003−6011.
(60) Zhou, G.; Chu, W.; Prezhdo, O. V. Structural Deformation Controls Charge Losses in $MAPbI_3$: Unsupervised Machine Learning of Nonadiabatic Molecular Dynamics. *ACS Energy Lett.* **2020**, *5*, 1930−1938.
(61) Mangan, S. M.; Zhou, G. Q.; Chu, W. B.; Prezhdo, O. V. Dependence Between Structural and Electronic Properties of $CsPbI_3$: Unsupervised Machine Learning of Nonadiabatic Molecular Dynamics. *J. Phys. Chem. Lett.* **2021**, *12*, 8672−8678.
(62) Huang, L. Y.; Lambrecht, W. R. L. Electronic Band Structure, Phonons, and Exciton Binding Energies of Halide Perovskites $CsSnCl_3$, $CsSnBr_3$, and $CsSnI_3$. *Phys. Rev. B: Condens. Matter Mater. Phys.* **2013**, *88*, 165203.
(63) Oga, H.; Saeki, A.; Ogomi, Y.; Hayase, S.; Seki, S. Improved Understanding of the Electronic and Energetic Landscapes of Perovskite Solar Cells: High Local Charge Carrier Mobility, Reduced Recombination, and Extremely Shallow Traps. *J. Am. Chem. Soc.* **2014**, *136*, 13818−13825.
(64) Savenije, T. J.; Ponseca, C. S.; Kunneman, L.; Abdellah, M.; Zheng, K. B.; Tian, Y. X.; Zhu, Q. S.; Canton, S. E.; Scheblykin, I. G.; Pullerits, T.; Yartsev, A.; Sundstrom, V. Thermally Activated Exciton Dissociation and Recombination Control the Carrier Dynamics in Organometal Halide Perovskite. *J. Phys. Chem. Lett.* **2014**, *5*, 2189−2194.
(65) Wright, A. D.; Verdi, C.; Milot, R. L.; Eperon, G. E.; Perez-Osorio, M. A.; Snaith, H. J.; Giustino, F.; Johnston, M. B.; Herz, L. M. Electron-Phonon Coupling in Hybrid Lead Halide Perovskites. *Nat. Commun.* **2016**, *7*, 11755.
(66) Li, W.; Tang, J. F.; Casanova, D.; Prezhdo, O. V. Time-Domain ab Initio Analysis Rationalizes the Unusual Temperature Dependence of Charge Carrier Relaxation in Lead Halide Perovskite. *ACS Energy Lett.* **2018**, *3*, 2713−2720.
(67) Domcke, W.; Yarkony, D. R. Role of Conical Intersections in Molecular Spectroscopy and Photoinduced Chemical Dynamics. *Annu. Rev. Phys. Chem.* **2012**, *63*, 325−352.
(68) Prezhdo, O. V.; Rossky, P. J. Evaluation of Quantum Transition Rates from Quantum-Classical Molecular Dynamics Simulations. *J. Chem. Phys.* **1997**, *107*, 5863−5878.
(69) Akimov, A. V.; Prezhdo, O. V. The PYXAID Program for Non-Adiabatic Molecular Dynamics in Condensed Matter Systems. *J. Chem. Theory Comput.* **2013**, *9*, 4959−4972.
(70) Itano, W. M.; Heinzen, D. J.; Bollinger, J. J.; Wineland, D. J. Quantum Zeno Effect. *Phys. Rev. A: At., Mol., Opt. Phys.* **1990**, *41*, 2295−2300.
(71) Facchi, P.; Nakazato, H.; Pascazio, S. From the Quantum Zeno to the Inverse Quantum Zeno Effect. *Phys. Rev. Lett.* **2001**, *86*, 2699−2703.
(72) Maniscalco, S.; Francica, F.; Zaffino, R. L.; Lo Gullo, N.; Plastina, F. Protecting Entanglement Via the Quantum Zeno Effect. *Phys. Rev. Lett.* **2008**, *100*, 090503.
(73) Kilina, S. V.; Neukirch, A. J.; Habenicht, B. F.; Kilin, D. S.; Prezhdo, O. V. Quantum Zeno Effect Rationalizes the Phonon Bottleneck in Semiconductor Quantum Dots. *Phys. Rev. Lett.* **2013**, *110*, 180404.
(74) Leguy, A. M. A.; Goni, A. R.; Frost, J. M.; Skelton, J.; Brivio, F.; Rodriguez-Martinez, X.; Weber, O. J.; Pallipurath, A.; Alonso, M. I.; Campoy-Quiles, M.; Weller, M. T.; Nelson, J.; Walsh, A.; Barnes, P. R. F. Dynamic Disorder, Phonon Lifetimes, and the Assignment of Modes to the Vibrational Spectra of Methylammonium Lead Halide Perovskites. *Phys. Chem. Chem. Phys.* **2016**, *18*, 27051−27066.
(75) Quarti, C.; Grancini, G.; Mosconi, E.; Bruno, P.; Ball, J. M.; Lee, M. M.; Snaith, H. J.; Petrozza, A.; De Angelis, F. The Raman Spectrum of the $CH_3NH_3PbI_3$ Hybrid Perovskite: Interplay of Theory and Experiment. *J. Phys. Chem. Lett.* **2014**, *5*, 279−284.
(76) Pistor, P.; Ruiz, A.; Cabot, A.; Izquierdo-Roca, V. Advanced Raman Spectroscopy of Methylammonium Lead Iodide: Development of a Non-destructive Characterisation Methodology. *Sci. Rep.* **2016**, *6*, 35973.
(77) Perez-Osorio, M. A.; Milot, R. L.; Filip, M. R.; Patel, J. B.; Herz, L. M.; Johnston, M. B.; Giustino, F. Vibrational Properties of the Organic Inorganic Halide Perovskite $CH_3NH_3PbI_3$ from Theory and Experiment: Factor Group Analysis, First-Principles Calculations, and Low-Temperature Infrared Spectra. *J. Phys. Chem. C* **2015**, *119*, 25703−25718.
(78) Mukamel, S. *Principles of Nonlinear Optical Spectroscopy*; Oxford University Press: Oxford, U.K., 1995.
(79) Akimov, A. V.; Prezhdo, O. V. Persistent Electronic Coherence Despite Rapid Loss of Electron-Nuclear Correlation. *J. Phys. Chem. Lett.* **2013**, *4*, 3857−3864.
(80) Li, L.; Long, R.; Prezhdo, O. V. Charge Separation and Recombination in Two-Dimensional MoS_2/WS_2: Time-Domain Ab Initio Modeling. *Chem. Mater.* **2017**, *29*, 2466−2473.
(81) Long, R.; Fang, W.; Akimov, A. V. Nonradiative Electron-Hole Recombination Rate Is Greatly Reduced by Defects in Monolayer Black Phosphorus: Ab Initio Time Domain Study. *J. Phys. Chem. Lett.* **2016**, *7*, 653−659.
(82) Kamisaka, H.; Kilina, S. V.; Yamashita, K.; Prezhdo, O. V. Ultrafast Vibrationally-Induced Dephasing of Electronic Excitations in PbSe Quantum Dots. *Nano Lett.* **2006**, *6*, 2295−2300.
(83) Chen, Y.; Wang, T.; Li, Z.; Li, H.; Ye, T.; Wetzel, C.; Li, H.; Shi, S.-F. Communicating Two States in Perovskite Revealed by Time-Resolved Photoluminescence Spectroscopy. *Sci. Rep.* **2018**, *8*, 16482.
(84) Greenland, C.; Shnier, A.; Rajendran, S. K.; Smith, J. A.; Game, O. S.; Wamwangi, D.; Turnbull, G. A.; Samuel, I. D. W.; Billing, D. G.; Lidzey, D. G. Correlating Phase Behavior with Photophysical Properties in Mixed-Cation Mixed-Halide Perovskite Thin Films. *Adv. Energy Mater.* **2019**, *10*, 1901350.
(85) Klein, J. R.; Flender, O.; Scholz, M.; Oum, K.; Lenzer, T. Charge Carrier Dynamics of Methylammonium Lead Iodide: From PbI_2-rich to Low-Dimensional Broadly Emitting Perovskites. *Phys. Chem. Chem. Phys.* **2016**, *18*, 10800−10808.
(86) Shi, R.; Long, R. Hole Localization Inhibits Charge Recombination in Tin-Lead Mixed Perovskites: Time-Domain ab Initio Analysis. *J. Phys. Chem. Lett.* **2019**, *10*, 6604−6612.
(87) Milot, R. L.; Eperon, G. E.; Snaith, H. J.; Johnston, M. B.; Herz, L. M. Temperature-Dependent Charge-Carrier Dynamics in $CH_3NH_3PbI_3$ Perovskite Thin Films. *Adv. Funct. Mater.* **2015**, *25*, 6218−6227.
(88) Munson, K. T.; Kennehan, E. R.; Doucette, G. S.; Asbury, J. B. Dynamic Disorder Dominates Delocalization, Transport, and Recombination in Halide Perovskites. *Chem* **2018**, *4*, 2826−2843.
(89) Trimpl, M. J.; Wright, A. D.; Schutt, K.; Buizza, L. R. V.; Wang, Z.; Johnston, M. B.; Snaith, H. J.; Müller-Buschbaum, P.; Herz, L. M. Charge-Carrier Trapping and Radiative Recombination in Metal Halide Perovskite Semiconductors. *Adv. Funct. Mater.* **2020**, *30*, 2004312.
(90) Ulatowski, A. M.; Wright, A. D.; Wenger, B.; Buizza, L. R. V.; Motti, S. G.; Eggimann, H. J.; Savill, K. J.; Borchert, J.; Snaith, H. J.; Johnston, M. B.; Herz, L. M. Charge-Carrier Trapping Dynamics in Bismuth-Doped Thin Films of $MAPbBr_3$ Perovskite. *J. Phys. Chem. Lett.* **2020**, *11*, 3681−3688.
(91) Li, W.; Vasenko, A. S.; Tang, J. F.; Prezhdo, O. V. Anharmonicity Extends Carrier Lifetimes in Lead Halide Perovskites at Elevated Temperatures. *J. Phys. Chem. Lett.* **2019**, *10*, 6219−6226.
(92) Zhan, J.; Yang, J.; Xie, X. Y.; Prezhdo, O. V.; Li, W. Interplay of Structural Fluctuations and Charge Carrier Dynamics is Key for High Performance of Hybrid Lead Halide Perovskites. *Inorg. Chem. Front.* **2022**, *9*, 5549−5561.
(93) Kresse, G.; Furthmuller, J. Efficient Iterative Schemes for Ab Initio Total-energy Calculations Using a Plane-Wave Basis Set. *Phys. Rev. B: Condens. Matter Mater. Phys.* **1996**, *54*, 11169−11186.
(94) Kresse, G.; Hafner, J. Ab-Initio Molecular-Dynamics for Open-Shell Transition-Metals. *Phys. Rev. B: Condens. Matter Mater. Phys.* **1993**, *48*, 13115−13118.

(95) Kapil, V.; Rossi, M.; Marsalek, O.; Petraglia, R.; Litman, Y.; Spura, T.; Cheng, B.; Cuzzocrea, A.; Meißner, R. H.; Wilkins, D. M.; Helfrecht, B. A.; Juda, P.; Bienvenue, S. P.; Fang, W.; Kessler, J.; Poltavsky, I.; Vandenbrande, S.; Wieme, J.; Corminboeuf, C.; Kühne, T. D.; Manolopoulos, D. E.; Markland, T. E.; Richardson, J. O.; Tkatchenko, A.; Tribello, G. A.; Van Speybroeck, V.; Ceriotti, M. i-PI 2.0: A Universal Force Engine for Advanced Molecular Simulations. *Comput. Phys. Commun.* **2019**, *236*, 214−223.
(96) Perdew, J. P.; Burke, K.; Ernzerhof, M. Generalized Gradient Approximation Made Simple [Phys. Rev. Lett. 77, 3865 (1996)]. *Phys. Rev. Lett.* **1997**, *78*, 1396.
(97) Blochl, P. E. Projector Augmented-Wave Method. *Phys. Rev. B: Condens. Matter Mater. Phys.* **1994**, *50*, 17953−17979.
(98) Grimme, S.; Antony, J.; Ehrlich, S.; Krieg, H. A Consistent and Accurate Ab Initio Parametrization of Density Functional Dispersion Correction (DFT-D) for the 94 Elements H-Pu. *J. Chem. Phys.* **2010**, *132*, 154104.
(99) Monkhorst, H. J.; Pack, J. D. Special Points for Brillouin-Zone Integrations. *Phys. Rev. B: Solid State* **1976**, *13*, 5188−5192.
(100) Rossi, M.; Ceriotti, M.; Manolopoulos, D. E. How to Remove the Spurious Resonances from Ring Polymer Molecular Dynamics. *J. Chem. Phys.* **2014**, *140*, 234116.
(101) Rossi, M.; Kapil, V.; Ceriotti, M. Fine Tuning Classical and Quantum Molecular Dynamics Using a Generalized Langevin Equation. *J. Chem. Phys.* **2018**, *148*, 102301.
(102) Chu, W. B.; Zheng, Q. J.; Akimov, A. V.; Zhao, J.; Saidi, W. A.; Prezhdo, O. V. Accurate Computation of Nonadiabatic Coupling with Projector Augmented-Wave Pseudopotentials. *J. Phys. Chem. Lett.* **2020**, *11*, 10073−10080.
(103) Chu, W. B.; Prezhdo, O. V. Concentric Approximation for Fast and Accurate Numerical Evaluation of Nonadiabatic Coupling with Projector Augmented-Wave Pseudopotentials. *J. Phys. Chem. Lett.* **2021**, *12*, 3082−3089.
(104) Akimov, A. V.; Prezhdo, O. V. Advanced Capabilities of the PYXAID Program: Integration Schemes, Decoherenc:e Effects, Multiexcitonic States, and Field-Matter Interaction. *J. Chem. Theory Comput.* **2014**, *10*, 789−804.
(105) Jaeger, H. M.; Fischer, S.; Prezhdo, O. V. Decoherence-Induced Surface Hopping. *J. Chem. Phys.* **2012**, *137*, 22A545.
(106) Kohn, W.; Sham, L. J. Self-Consistent Equations Including Exchange and Correlation Effects. *Phys. Rev.* **1965**, *140*, A1133−A1138.
(107) Craig, C. F.; Duncan, W. R.; Prezhdo, O. V. Trajectory Surface Hopping in the Time-Dependent Kohn-Sham Approach for Electron-Nuclear Dynamics. *Phys. Rev. Lett.* **2005**, *95*, 163001.
(108) Prezhdo, O. V. Mean Field Approximation for the Stochastic Schrodinger Equation. *J. Chem. Phys.* **1999**, *111*, 8366−8377.
(109) Cheng, C.; English, N. J.; Fang, W.-H.; Long, R. Understanding Competitive Photo-Induced Molecular Oxygen Dissociation and Desorption Dynamics atop a Reduced Rutile TiO_2(110) Surface: A Time-Domain Ab Initio Study. *ACS Catal.* **2022**, *12*, 6702−6711.
(110) Cheng, C.; Zhu, Y.; Zhou, Z.; Long, R.; Fang, W.-H. Photoinduced Small Electron Polarons Generation and Recombination in Hematite. *npj Comput. Mater.* **2022**, *8*, 148.
(111) Cheng, C.; Fang, Q.; Fernandez-Alberti, S.; Long, R. Depleted Oxygen Defect State Enhancing Tungsten Trioxide Photocatalysis: A Quantum Dynamics Perspective. *J. Phys. Chem. Lett.* **2022**, *13*, 5571−5580.
(112) Wang, H.; Zhou, Z. H.; Long, R.; Prezhdo, O. V. Passivation of Hematite by a Semiconducting Overlayer Reduces Charge Recombination: An Insight from Nonadiabatic Molecular Dynamics. *J. Phys. Chem. Lett.* **2023**, *14*, 879−887.
(113) Yang, Y. T.; Fang, W. H.; Benderskii, A.; Long, R.; Prezhdo, O. V. Strain Controls Charge Carrier Lifetimes in Monolayer WSe_2: Ab Initio Time Domain Analysis. *J. Phys. Chem. Lett.* **2019**, *10*, 7732−7739.
(114) Wang, X. L.; Long, R. Oxidation Notably Accelerates Nonradiative Electron-Hole Recombination in MoS_2 by Different Mechanisms: Time-Domain Ab Initio Analysis. *J. Phys. Chem. Lett.* **2020**, *11*, 4086−4092.
(115) Li, L. Q.; Long, R.; Prezhdo, O. V. Why Chemical Vapor Deposition Grown MoS_2 Samples Outperform Physical Vapor Deposition Samples: Time-Domain ab Initio Analysis. *Nano Lett.* **2018**, *18*, 4008−4014.
(116) Zhu, Y. H.; Fang, W. H.; Rubio, A.; Long, R.; Prezhdo, O. V. The Twist Angle has Weak Influence on Charge Separation and Strong Influence on Recombination in the MoS_2/WS_2 Bilayer: Ab Initio Quantum Dynamics. *J. Mater. Chem. A* **2022**, *10*, 8324−8333.
(117) Zhang, Z. S.; Fang, W. H.; Long, R.; Prezhdo, O. V. Exciton Dissociation and Suppressed Charge Recombination at 2D Perovskite Edges: Key Roles of Unsaturated Halide Bonds and Thermal Disorder. *J. Am. Chem. Soc.* **2019**, *141*, 15557−15566.
(118) Shi, R.; Zhang, Z. S.; Fang, W. H.; Long, R. Charge Localization Control of Electron-Hole Recombination in Multilayer Two-Dimensional Dion-Jacobson Hybrid Perovskites. *J. Mater. Chem. A* **2020**, *8*, 9168−9176.
(119) Shi, R.; Long, R.; Fang, W. H.; Prezhdo, O. V. Rapid Interlayer Charge Separation and Extended Carrier Lifetimes due to Spontaneous Symmetry Breaking in Organic and Mixed Organic-Inorganic Dion-Jacobson Perovskites. *J. Am. Chem. Soc.* **2023**, *145*, 5297−5309.
(120) Tong, C. J.; Li, L. Q.; Liu, L. M.; Prezhdo, O. V. Synergy between Ion Migration and Charge Carrier Recombination in Metal-Halide Perovskites. *J. Am. Chem. Soc.* **2020**, *142*, 3060−3068.
(121) Lu, T. F.; Gumber, S.; Tokina, M. V.; Tomko, J. A.; Hopkins, P. E.; Prezhdo, O. V. Electron-Phonon Relaxation at the Au/WSe_2 Interface is Significantly Accelerated by a Ti Adhesion Layer: Time-Domain Ab Initio Analysis. *Nanoscale* **2022**, *14*, 10514−10523.
(122) Agrawal, S.; Vasenko, A. S.; Trivedi, D. J.; Prezhdo, O. V. Charge Carrier Nonadiabatic Dynamics in Non-Metal Doped Graphitic Carbon Nitride. *J. Chem. Phys.* **2022**, *156*, 094702.

https://doi.org/10.1021/jacs.3c04412
J. Am. Chem. Soc. 2023, 145, 14112−14123